REFERENCES

[1] S. R. Taub and S. A. Alterovitz, "Silicon technologies adjust to RF applications," *Microwaves & RF*, pp. 60–74, Oct. 1994.

[2] A. K. Agarwal *et al.*, "MICROX—an advanced silicon technology from microwave circuits up to x-band," in *Proc. 1991 IEEE Int. Electron Devices Meeting*, pp. 687–690.

[3] T. M. Hyltin, "Microstrip transmission on semiconductor dielectrics," *IEEE Trans. Microwave Theory Tech.*, vol. MTT-13, no. 6, pp. 777–780, Nov. 1965.

[4] A. Rosen *et al.*, "Silicon as a millimeter-wave monolithically integrated substrate—a new look," *RCA Rev.*, vol. 42, pp. 633–660, 1981.

[5] S. R. Taub and P. Young, "Temperature dependent performance of coplanar waveguide (CPW) on substrates of various materials," *Proc. 1994 IEEE MTT-S Int. Microwave Symp.*, pp. 1049–1051, May 1994.

[6] *Atlas User's Manual*, 2nd ed., Silvaco International, Mar. 1, 1994.

[7] S. Wolf and R. N. Tauber, *Silicon Processing for the VLSI Era, Volume 1: Process Technology*. Sunset Beach, CA: Lattice, 1986, pp. 176–177.

Spectral Domain Analysis of Single and Coupled Microstrip Open Discontinuities with Anisotropic Substrates

Jaideva C. Goswami, Andrew K. Chan, and Charles K. Chui

Abstract— **The normalized input admittance for single and coupled microstrip open discontinuities with anisotropic substrates are obtained using a full-wave analysis. Problem is formulated in terms of the field Green's function in the spectral domain. Numerical results are found to be in good agreement with the published theoretical and experimental results for microstrip open discontinuities with anisotropic/isotropic substrates.**

I. INTRODUCTION

Extensive research related to discontinuities in planar transmission lines with isotropic substrates has been carried out. However, results for the propagation characteristics and discontinuity effects of transmission lines with anisotropic substrates are scant. In fact, there seems to be only one paper [1] that deals with microstrip open discontinuity on anisotropic substrates. In [1], a dynamic source reversal method based on potential theory has been used to compute open circuit capacitance. The microstrip is enclosed in a waveguide of infinite extent, operating in its cut-off mode.

The objective of this paper is to analyze the end effects of single and coupled microstrip open discontinuities with uniaxial substrates using spectral domain method. The analysis presented in the paper can be reduced to the isotropic case with some trivial modifications. Furthermore, it can be extended to slot line and CPW line by using appropriate Green's function. The paper is organized as follows. In the next section we discuss the formulation of the problem for coupled microstrip line which can be easily modified for single line. There are a couple of papers that deal with the Green's function in uniaxial medium. We avoid repeating the derivation by giving proper reference. The real-axis integration method is used to evaluate various integrals involved in the formulation. For this purpose, we provide the expressions for the asymptotic form, poles and residues of the Green's function in Sections II and III. In Section IV, we discuss the numerical results and compare them with the published ones. Finally, we conclude our work in Section V.

Manuscript received September 14, 1995; revised March 20, 1996. This work was supported in part by the Texas Higher Education Coordinating Board under Grants 999903-066 and 999903-067.

J. C. Goswami is with the Electromagnetic Communication Laboratory, University of Illinois at Urbana-Champaign, IL 61801 USA.

A. K. Chan is with the Electromagnetics and Microwave Laboratory, Department of Electrical Engineering, Texas A&M University, College Station, TX 77843-3128 USA.

C. K. Chui is with the Center for Approximation Theory, Department of Mathematics, Texas A&M University, College Station, TX 77843-3368 USA.

Publisher Item Identifier S 0018-9480(96)04727-8.

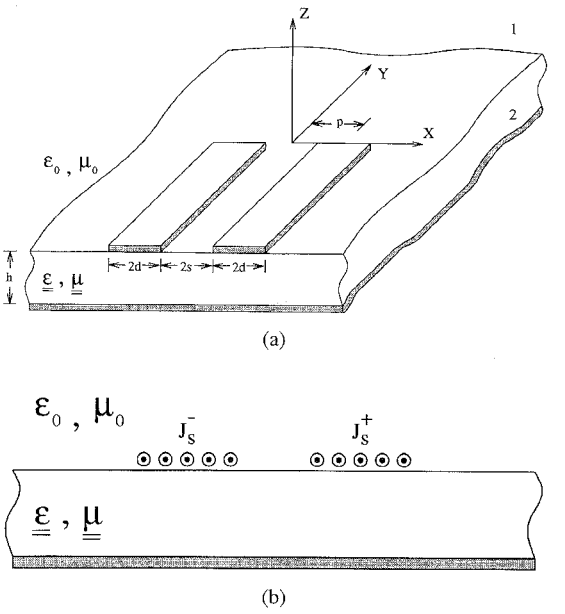

Fig. 1. (a) Open coupled-microstrip and (b) the equivalent problem.

II. FORMULATION

Transmission line configuration to be studied is shown in Fig. 1(a). We assume that the metal thickness is zero and that the substrate is lossless. Observe that the configuration shown in Fig. 1(a) reduces to that of a single microstrip line for $p = 0$.

We will use field integral equations in spectral domain for the purpose of analysis. Although we provide results for dielectric anisotropy only, let us, for a general case, consider that the substrate is characterized by both the relative permittivity and permeability tensors, given as

$$\underline{\underline{\epsilon}} = \underline{\underline{\mathbf{I}}}_t \epsilon_t + \hat{\mathbf{z}}\hat{\mathbf{z}}\epsilon_z, \quad \underline{\underline{\mu}} = \underline{\underline{\mathbf{I}}}_t \mu_t + \hat{\mathbf{z}}\hat{\mathbf{z}}\mu_z \tag{1}$$

where $\underline{\underline{\mathbf{I}}}_t$ is the identity dyadic, transverse to the optic axis $\hat{\mathbf{z}}$. Let the electric and magnetic anisotropy ratios ν^e and ν^h be defined as

$$\nu^e = \frac{\epsilon_t}{\epsilon_z}, \quad \nu^h = \frac{\mu_t}{\mu_z}. \tag{2}$$

For the medium characterized by (1), the time-harmonic form of the Maxwell's equation becomes

$$-\nabla \times \mathbf{E} = j\omega\mu_0 \underline{\underline{\mu}} \cdot \mathbf{H} + \mathbf{M} \tag{3}$$

$$\nabla \times \mathbf{H} = j\omega\epsilon_0 \underline{\underline{\epsilon}} \cdot \mathbf{E} + \mathbf{J}. \tag{4}$$

The dyadic electric field Green's function $\underline{\underline{\mathbf{G}}}^{EJ}(\mathbf{r}, \mathbf{r}')$ can be obtained from (3) and (4) in terms of the transmission line Green's function [2, Ch. 2]. A detail description of such formulation is given in [3].

In the present analysis, first, we replace the strip regions by equivalent surface electric current (see Fig. 1(b)), namely

$$\mathbf{J}_s(\mathbf{r}) = \hat{\mathbf{z}} \times \mathbf{H}(\mathbf{r}); \quad \mathbf{r} \in \mathcal{D} := \mathcal{D}^+ \cup \mathcal{D}^- \tag{5}$$

where $\mathcal{D}^+ := \{x, y, z \mid x \in (s, s+2d), y \in (-\infty, 0], z = 0\}$ and $\mathcal{D}^- := \{x, y, z \mid x \in (-s, -s-2d), y \in (-\infty, 0], z = 0\}$ and then obtain the electric field integral equation by enforcing the boundary condition

$$\hat{\mathbf{z}} \times \mathbf{E}(\mathbf{r}) = 0; \quad \mathbf{r} \in \mathcal{D}. \tag{6}$$

At this stage, we assume that the strip-width is very small compared to the operating wavelength and, consequently, only y components of the electric field and current exist. Let us assume that the surface electric current distribution has the following functional dependence on x and y

$$J^+_{s,y}(x,y) = f^+_x(x) f_y(y); (x,y) \in \mathcal{D}^+ \tag{7}$$

$$J^-_{s,y}(x,y) = f^-_x(x) f_y(y); (x,y) \in \mathcal{D}^-. \tag{8}$$

Since the strip-width is very small compared with the operating wavelength, we take one-term approximation of the x-dependence of the electric current. Based on the edge-condition, we represent $f^+_x(x)$ and $f^-_x(x)$ as

$$f^+_x(x) = g(x-p), f^-_x(x) = \pm g(x+p); \tag{9}$$

$$g(x) = \frac{1}{\pi\sqrt{d^2 - x^2}}, \tag{10}$$

$$\hat{g}(k_x) = J_0(k_x d). \tag{11}$$

In (9), plus and minus signs preceding $g(x+p)$, apply to even and odd modes, respectively; $\hat{g}(k_x)$ represents the Fourier transform of $g(x)$, and, in (11), J_0 is the zero order first-kind Bessel function.

By choosing a suitable testing function which has the same x-dependence as (9) and y-dependence as $\phi_k(y)$ for some integer k and by applying the boundary condition (6), we have

$$\int_{-\infty}^{\infty}\int_{-\infty}^{\infty} \Lambda^{EJ}(k_x, k_y) \hat{f}_y(k_y) \hat{\phi}_k(-k_y) dk_x dk_y = 0 \tag{12}$$

where

$$\Lambda^{EJ}(k_x, k_y) = \hat{G}^{EJ}_{yy}(k_x, k_y) J_0^2(k_x d) \begin{Bmatrix} \cos^2(k_x p) \\ \sin^2(k_x p) \end{Bmatrix} \tag{13}$$

with $\cos^2(k_x p)$ and $\sin^2(k_x p)$ for even and odd modes, respectively. In order to find the propagation constant, k_{ye}, of the infinite transmission line, we assume that all the field and current distributions have their y-dependence as $e^{-jk_{ye}y}$. It is easy, for this case, to arrive at

$$\int_{-\infty}^{\infty} \Lambda^{EJ}(k_x, k_{ye}) dk_x = 0. \tag{14}$$

Explicit expression for $\hat{G}^{EJ}_{yy}$ is given in [4]. To accelerate the convergence of the numerical integration, we need the asymptotic form of Λ^{EJ} as given below

$$\lim_{k_x \to \infty} \Lambda^{EJ}(k_x, k_y) =: \Lambda^{EJ}_{\infty}(k_x, k_y)$$
$$= j\frac{\eta_0}{\pi k_0 d k_x^2}\left[k_y^2 \frac{1}{1+p_e} - k_0^2 \frac{p_h}{1+p_h}\right] \times [1 + \sin(2k_x d)] \begin{Bmatrix} \cos^2(k_x p) \\ \sin^2(k_x p) \end{Bmatrix}, \tag{15}$$

where $p_e = \sqrt{\epsilon_t \epsilon_z}$ and $p_h = \sqrt{\mu_t \mu_z}$.

A. Longitudinal Variation of Current

Since the transverse dimensions of strips are very small compared with the wavelength, we assume that the current distribution, sufficiently away from the discontinuity, is due to the fundamental mode only. Near the discontinuity, in addition to the entire domain basis functions representing the fundamental mode, subdomain basis functions are used to expand the unknown current to account for the deviation caused by the presence of higher order modes generated by the discontinuity. For subdomain basis functions, we use piecewise sinusoids (PWS). With these, the longitudinal variation of current is given as

$$f_y(y) = s_i(y) - \Gamma s_r(y) + \sum_{k=0}^{K} c_k \phi_k(y), \quad K > 0. \tag{16}$$

The entire domain functions s_i and s_r, representing incident and reflected waves, respectively, are given below [5]

$$s_i(y) := \cos(k_{ye}y) U\left(-y - \frac{\pi}{2k_{ye}}\right) - j\sin(k_{ye}y) U(-y), \tag{17}$$

$$\hat{s}_i(k_y) = \left\{\exp\left(-j\frac{\pi k_y}{2k_{ye}}\right) - j\right\} \times \left[\frac{k_{ye}}{k_y^2 - k_{ye}^2} + j\frac{\pi}{2}\left[\delta(k_y - k_{ye}) - \delta(k_y + k_{ye})\right]\right] \tag{18}$$

$$s_r(y) := \cos(k_{ye}y) U\left(-y - \frac{\pi}{2k_{ye}}\right) + j\sin(k_{ye}y) U(-y), \tag{19}$$

$$\hat{s}_r(k_y) = \left\{\exp\left(-j\frac{\pi k_y}{2k_{ye}}\right) + j\right\} \times \left[\frac{k_{ye}}{k_y^2 - k_{ye}^2} + j\frac{\pi}{2}\left[\delta(k_y - k_{ye}) - \delta(k_y + k_{ye})\right]\right] \tag{20}$$

where k_{ye} is the propagation constant for the fundamental mode and $U(y)$ is the Heaviside function, defined in a usual way as

$$U(y) = \begin{cases} 1 & y \geq 0; \\ 0 & y < 0. \end{cases} \tag{21}$$

The subdomain basis function ϕ_k for piecewise sinusoid case is

$$\phi_k(y) := \cap(y + \tau(k+1)) \tag{22}$$

$$\cap(y) := \begin{cases} \frac{\sin(k_{ye}(\tau - |y|))}{\sin(k_{ye}\tau)} & |y| \leq \tau, \\ 0 & \text{elsewhere;} \end{cases} \tag{23}$$

$$\hat{\phi}_k(k_y) = e^{-j\tau(k+1)k_y} \frac{2k_{ye}}{k_y^2 - k_{ye}^2} \times \frac{\cos(k_{ye}\tau) - \cos(k_y\tau)}{\sin(k_{ye}\tau)} \tag{24}$$

with $0 < \tau < \frac{\pi}{2k_{ye}}$.

III. Surface-Wave Poles

In this section we are concerned with the evaluation of surface-wave poles that must be taken into account while integrating along the real-axis in the complex k_x-plane. We will use graphical methods [6], [7] to obtain these poles. In the k_ρ-plane ($k_\rho^2 = k_x^2 + k_y^2$), surface-wave poles lie in $[k_1, k_2]$ where $k_1 = k_0$ and $k_2 = \max\{k_0\sqrt{\mu_t\epsilon_z}, k_0\sqrt{\mu_z\epsilon_t}\}$. The following parameters, with their usual meaning, will be required in our subsequent discussion

$$k_z^p = \begin{cases} \sqrt{k_t^2 - \nu^p k_\rho^2}; & k_t^2 \geq \nu^p k_\rho^2 \\ -j\sqrt{\nu^p k_\rho^2 - k_t^2}; & k_t^2 \leq \nu^p k_\rho^2 \end{cases} \tag{25}$$

$$k_t = k_0\sqrt{\mu_t\epsilon_t}; \quad k_0 = \omega\sqrt{\mu_0\epsilon_0} \tag{26}$$

$$\eta_t = \eta_0\sqrt{\mu_t/\epsilon_t}; \quad \eta_0 = \sqrt{\mu_0/\epsilon_0} \tag{27}$$

where $p = e, h$ imply TM and TE cases, respectively.

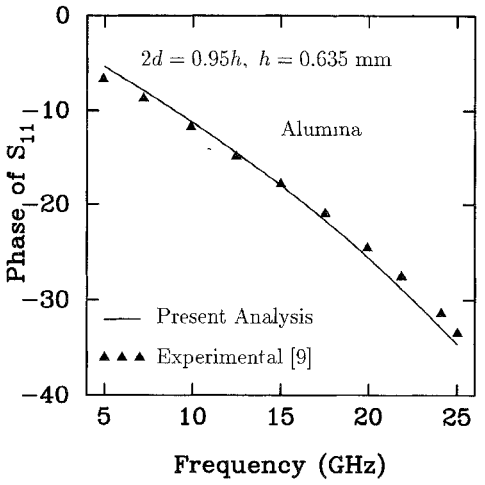

Fig. 2. Comparison of results for phase of the scattering parameter S_{11} of open microstrip line with alumina ($\epsilon_t = \epsilon_r = 9.9$) substrate

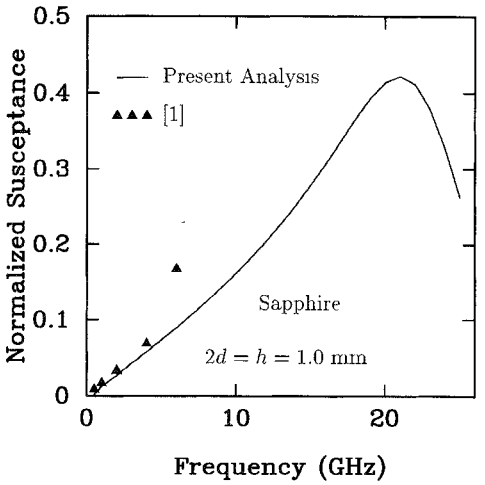

Fig. 3. Comparison of results for normalized input susceptance of open microstrip line with sapphire substrate.

A. TE Surface-Wave Poles

For TE case, surface-wave poles are obtained by solving the transcendental equation

$$k_{z2}^h h = (n-1)\pi + \frac{\pi}{2} + \arctan\left[\frac{k_0 p_h r_h \sqrt{1-\left(\frac{k_{z2}^h}{k_0 r_h}\right)^2}}{k_{z2}^h}\right] \quad (28)$$

where $r_h = \sqrt{\mu_t \epsilon_t - \nu^h}$ and $n = 1, 2, \ldots$. First we find roots of (28) in the k_{z2}-plane and then map these poles to the k_x-plane using (25). On the k_{z2}-plane the nth root of (28) lies in $[L_h, U_h]$, where

$$L_h = \frac{2n\pi k_0 r_h}{\pi + 2hk_0 r_h}, \quad U_h = \min\left\{\frac{n\pi}{h}, k_0 r_h\right\}; \; n = 1, 2, \ldots. \quad (29)$$

Total number (N_h) of TE–surface-wave poles, for a given substrate thickness, is

$$N_h = \left\lfloor \frac{1}{2} + \frac{2hr_h}{\lambda_0} \right\rfloor \quad (30)$$

where $\lfloor x \rfloor$ is the largest integer that is smaller than or equal to x.

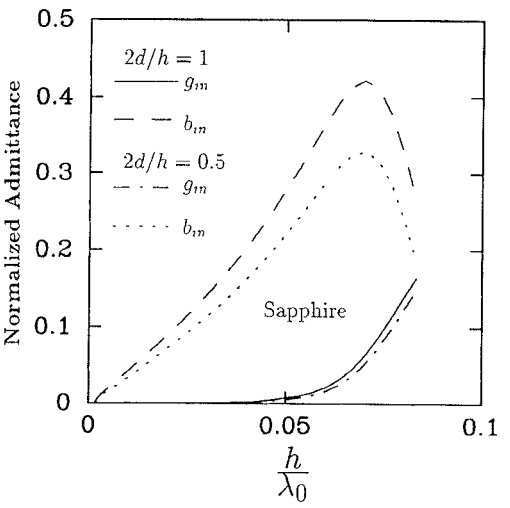

Fig 4. Results for normalized input susceptance (b_{in}) and conductance (g_{in}) of open microstrip line with sapphire substrate.

Expression for residue $R_i^{EJ,h}$ of G_{yy}^{EJ} at a pole p_x on the k_x-plane is given below

$$R_i^{EJ,h}(k_y) = \mu_t \eta_0 k_0 \times \frac{p_x k_{z1}^h \left(k_{z2}^h\right)^2}{k_\rho^2} \times \frac{1}{\mu_t k_0^2 r_h^2 + j\nu^h h k_{z1}^h \left[\left(k_{z2}^h\right)^2 - \mu_t^2 \left(k_{z1}^h\right)^2\right]} \quad (31)$$

where k_{z1}^h, k_{z2}^h, and k_ρ are evaluated at $k_x = p_x$. Observe that since at a pole k_{z1}^h is imaginary and k_{z2}^h is real, the residues are purely imaginary.

B. TM Surface-Wave Poles

For TM case, the transcendental equation takes the form

$$k_{z2}^e h = (n-1)\pi + \arctan\left[\frac{k_0 p_e r_e \sqrt{1-\left(\frac{k_{z2}^e}{k_0 r_e}\right)^2}}{k_{z2}^e}\right] \quad (32)$$

where $r_e = \sqrt{\mu_t \epsilon_t - \nu^e}$ and $n = 1, 2, \ldots$ As done for the case with TE surface-wave pole, first we find roots of (32) in the k_{z2}-plane and then map these poles to the k_x-plane using (25). On the k_{z2}-plane the nth root of (32) lies in $[L_e, U_e]$, where

$$L_e = \frac{2n\pi k_0 r_e}{\pi + 2hk_0 r_e}, \quad U_e = \min\left\{\frac{n\pi}{h}, k_0 r_e\right\}; \quad n = 1, 2, \ldots. \quad (33)$$

Total number (N_e) of TM–surface-wave poles, for a given substrate thickness, is

$$N_e = \left\lfloor 1 + \frac{2hr_e}{\lambda_0} \right\rfloor. \quad (34)$$

Expression for residue $R_x^{EJ,e}$ of G_{yy}^{EJ} at a pole p_x on the k_x-plane are given below

$$R_x^{EJ,e}(k_y) = \frac{\epsilon_t \eta_0}{k_0} \times \frac{\left(k_{z1}^e\right)^3 \left(k_{z2}^e\right)^2}{p_x k_\rho^2} \times \frac{1}{\epsilon_t k_0^2 r_e^2 + j\nu^e h k_{z1}^e \left[\left(k_{z2}^e\right)^2 - \mu_t^2 \left(k_{z1}^e\right)^2\right]} \quad (35)$$

where k_{z1}^e, k_{z2}^e, and k_ρ are evaluated at $k_x = p_x$.

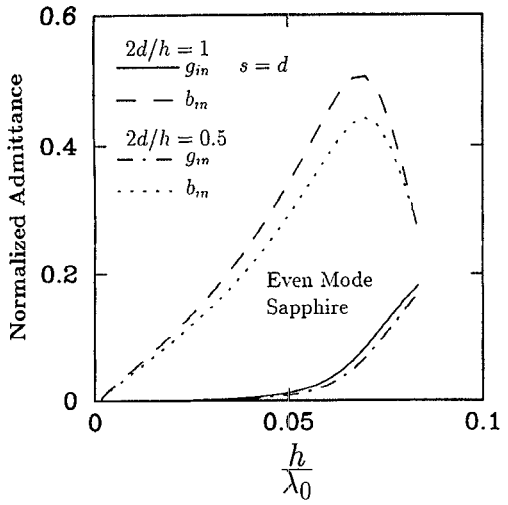

Fig. 5. Results for normalized input susceptance and conductance of open coupled-microstrip line (even mode) with sapphire substrate.

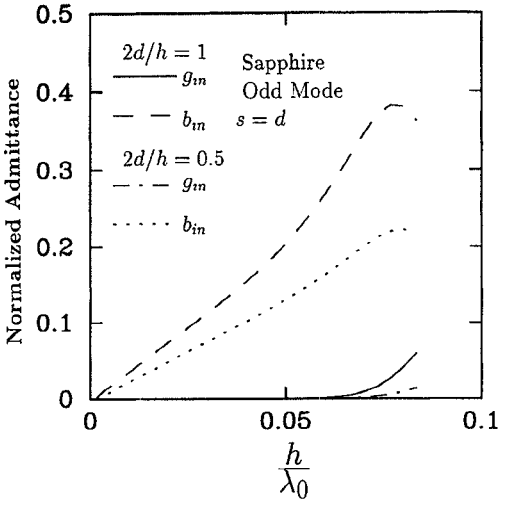

Fig. 6. Results for normalized input susceptance and conductance of open coupled-microstrip line (odd mode) with sapphire substrate.

It is worth mentioning here that for isotropic substrates in which $\nu_e = \nu_h = 1$, $p_e = p_h$, and $r_e = r_h$, TM and TE surface-wave poles alternate beginning with TM_0. However, such a pattern may not exist for uniaxial substrates.

IV. Numerical Results

Application of Petrov-Galerkin method with the basis functions described before leads to a set of linear equations, solution of which gives the desired value of the reflection coefficient Γ. The matrix structure is shown below

$$[[A_{p,1}] \quad [A_{p,q}]] \begin{bmatrix} \Gamma \\ [c_k] \end{bmatrix} = [B_p] \tag{36}$$

where the matrix elements take the form as

$$A_{p,1} = \frac{4k_{ye}^2}{\sin(k_{ye}\tau)} \int_0^\infty \int_0^\infty \Lambda^{EJ}(k_x, k_y) \times \frac{[\cos(k_{ye}\tau) - \cos(k_y\tau)]\left[\cos\left(\tau p - \frac{\tau}{2k_{ye}}\right)k_y + j\cos(\tau p k_y)\right]}{\left(k_y^2 - k_{ye}^2\right)^2} \times dk_x dk_y, \tag{37}$$

$$A_{p,q} = \frac{8k_{ye}^2}{\sin^2(k_{ye}\tau)} \int_0^\infty \int_0^\infty \Lambda^{EJ}(k_x, k_y) \times \frac{[\cos(k_{ye}\tau) - \cos(k_y\tau)]^2 \cos[(p-q+1)\tau k_y]}{\left(k_y^2 - k_{ye}^2\right)^2} \times dk_x dk_y, \tag{38}$$

$$B_p = \overline{A_{p,1}}, \tag{39}$$

with $p = 1, \ldots, M+2$, $q = 2, \ldots, M+2$, and $\overline{A_{p,1}}$, denoting complex conjugate of $A_{p,1}$. It is easy to verify that

$$A_{p,q} = A_{q-1,p+1}; \quad p = 1, \ldots, M+1, \tag{40}$$

$$A_{p,q} = A_{p-1,q-1}; \quad p = 2, \ldots, M+2; q = 3, \ldots, M+2 \tag{41}$$

indicating the symmetry and Toeplitz nature of the major portion of the matrix.

Integration over k_x is common to all the matrix elements, therefore, they need to be computed only once. Usually, this integration consumes most of the CPU time during the numerical evaluation. We use the real-axis integration [8] for the purpose of evaluating integrals of the matrix elements. We perform the integration by replacing Λ^{EJ} with $\Lambda^{EJ} - \Lambda^{EJ}_{\text{sing}} - \Lambda^{EJ}_{\infty}$ and then adding the integrals of the singular part, $\Lambda^{EJ}_{\text{sing}}$, and the asymptotic part, Λ^{EJ}_{∞}. Singularity subtraction smoothes the integrand while asymptotic subtraction accelerates the convergence. The discontinuity in the derivative at the branch point can be taken care of by trigonometric/hyperbolic transformation.

All the numerical results have been obtained using SPARC Server 1000 machine. As the first step toward validating our results, we have computed the the effective dielectric constant for different transmission line configurations and found excellent agreement with the published results. It takes less than 1 second to evaluate k_{ye} for one frequency. In Fig. 2, the phase of the scattering parameter S_{11} of a microstrip open discontinuity with alumina substrate, calculated using the present analysis, is compared with the experimental result [9]. Once again, we get very good agreement. For microstrip discontinuity with sapphire substrate, our results, as shown in Fig. 3, match fairly well with those in [1][1] for lower frequencies. At 6 GHz, however, results deviate quite significantly. This may be attributed to the fact that the results in [1] were obtained by placing the microstrip inside a rectangular waveguide which was supposed to be at cut-off. At higher frequencies the effect of the rectangular waveguide would become significant. Normalized susceptance (b_{in}) and conductance (g_{in}) for single and coupled microstrip transmission lines with sapphire substrate are shown in Figs. 4–6. For Figs. 4–6, 39 PWS function with $\tau = 0.018\,75\lambda_g$ were used. Computation time changes with h/λ_0. A typical CPU time for $h/\lambda_0 = 0.05$ is about 5 minutes.

V. Conclusion

In this paper we have analyzed open discontinuities in microstrip and coupled microstrip lines with uniaxial substrates. The analysis is quite general and can be used for isotropic case by simply setting $\mu_t = \mu_z$, and $\epsilon_t = \epsilon_z$. The analysis can also be extended to slot line and CPW line by replacing G^{EJ}_{yy} by G^{HM}_{yy} and making some simple changes in the formulation.

References

[1] S. S. Toncich, R. E. Collin, and K. B. Bhasin, "Full-wave characterization of microstrip open end discontinuities patterned on anisotropic

[1] In [1], w/h stands for the ratio of the total strip-width over the substrate-height [10]. This fact is not clear from [1].

substrate using potential theory," *IEEE Trans. Microwave Theory Tech.*, vol. 41, pp. 2067–2073, Dec. 1993.
[2] L B. Felsen and N. Marcuvitz, *Radiation and Scattering of Waves*. New York: IEEE, 1994.
[3] K A. Michalski, "Formulation of mixed-potential integral equations for arbitrarily shaped microstrip structures with uniaxial substrate," *J. Electromagn. Waves Applicat.*, vol. 7, pp. 899–917, 1993.
[4] J. C Goswami, "Applications of semi-orthogonal spline wavelets in electromagnetics and microwave problems," Ph D dissertation, Texas A&M Univ., College Station, TX, Aug. 1995
[5] T. S Horng, N. G. Alexópoulos, S. C Wu, and H Y. Yang, "Full-wave spectral-domain analysis for open microstrip discontinuities of arbitrary shape including radiation and surface-wave losses," *Int. J. Microwave Millimeter-Wave Computer-Aided Eng*., vol. 2, pp 224–240, 1992.
[6] A K. Bhattacharyya, "Approximate formulae for the surface wave numbers in a grounded dielectric structure," *Microwave Opt. Technol Lett*., vol. 3, pp 169–172, 1990
[7] C I. G. Hsu, R F Harrington, and K A Michalski, "On the mode spectrum of a parallel-plate waveguide filled with a two-layer uniaxial medium," *Microwave Opt Technol. Lett.*, vol. 5, pp 318–321, 1992.
[8] J. R. Mosig, "Integral equation technique," in *Numerical Techniques for Microwave and Millimeter-Wave Passive Structures*, T Itoh Ed., New York: Wiley, 1989, pp. 133–213.
[9] G. Gronau and I. Wolff, "A simple broad-band device de-embedding method using and automatic network analyzer with time-domain option," *IEEE Trans. Microwave Theory Tech.*, vol. 37, pp. 479–483, Mar. 1989.
[10] R. E. Collin, private communication.

Development of Accurate On-Wafer, Cryogenic Characterization Techniques

J. Laskar, J. J. Bautista, M. Nishimoto, M. Hamai, and R. Lai

***Abstract*— Significant advances in the development of high electron mobility field-effect transistors (HEMT's) have resulted in cryogenic, low-noise amplifiers (LNA's) whose noise temperatures are within an order of magnitude of the quantum noise limit ($h\nu/k$). Further advances in HEMT technology at cryogenic temperatures may eventually lead to the replacement of maser and superconducting-insulator-superconducting (SIS) front-ends in the 1–100 GHz frequency band. Key to identification of the best HEMT's and optimization of cryogenic LNA's is accurate and repeatable device measurements at cryogenic temperatures. A cryogenic on-wafer noise and scattering parameter measurement system has been developed to provide a syst**

ematic investigation of HEMT noise characteristics. In addition, an improved parameter extraction technique has been developed to help understand the relationship between device structure and LNA performance.

I. Introduction

As the demands for high performance satellite transmit/receive components increase, researchers have looked for viable alternatives to increase signal to noise margins at higher frequencies. Notable results have included the development of cryogenic low-noise amplifiers at X- and Ka-bands [1], [2] and the development of hybrid high temperature superconductor and semiconductor components [3]. The improvement of high performance satellite links and the need for high performance light satellites has provided the impetus for continued development and understanding of cryogenic microwave components. A critical element in the application of this technology is the development of a robust on-wafer characterization technique at cryogenic temperatures.

In recent years, significant progress has been made in the development of cryogenic, on-wafer probing systems [4]–[10]. The major shortcoming of previous efforts has been the lack of a repeatable and accurate system yielding results comparable to room temperature systems.

In this paper, we report a quantitative investigation in the accuracy of on-wafer cryogenic noise and S-parameter measurements. Results shown in this paper include:

1) demonstration of two-tier cryogenic calibrations;
2) study of the effect of temperature on calibration repeatability;
3) development of improved parameter extraction techniques for cryogenic temperatures;
4) investigation of room temperature noise techniques applied at cryogenic temperatures;
5) initial results of an on-chip cryogenic noise technique.

II. Cryogenic-Probe Measurement System

A variety of test fixtures have been used [4]–[9] to evaluate HEMT performance from 300 K to 15 K. Most of these fixtures are similar to the one developed by Liechti and Larrick [10], a microwave test fixture that could be immersed in liquid nitrogen. To date, it has been difficult to make broad band scattering (S)-parameter measurements in such an environment due to the limited accuracy of the full two-port calibrations.

The cryogenic microwave system in this work uses coplanar waveguide probes in a vacuum station coupled to a vector network analyzer for scattering parameter measurements, and a noise and test set with a noise system for microwave noise parameter measurements. The microwave measurement system currently under development incorporates measurement tools originally developed for the first system in 1989 [11], [12]. The cryogenic probe measurement system contains ports for RF cables, thermometers, vacuum pumps, dry nitrogen backfill lines, coplanar probes with manipulators, and a closed-cycle refrigerator cold head. The probe body rests on a copper block attached to a fiberglass post. The fiberglass reduces the thermal load and copper braiding from the cold head thermally anchors the probe to the 12 K cold station assuring sample temperatures of 12–20 K. The mechanical and thermal stability of the wafer stage is established by supporting it on fiberglass posts above the cold head and thermally anchoring it to the cold station with flexible copper braids.

The most important feature of this design is the incorporation of a closed-cycle helium refrigeration system. The first successful designs of on-wafer cryogenic systems used open-cycle cooling to reduce start up costs and avoid mechanical vibrations. However, for long term temperature stability, a closed-cycle helium source provides the optimum solution. Decoupling and damping of the vibrations from the cold head to the probe station is accomplished with a bellows and vibration mount. This system allows small-signal microwave measurements from DC to 40 GHz over a physical temperature range of 16–300 K. Since the microwave hardware is insulated by vacuum

Manuscript received September 22, 1995; revised March 20, 1996

J. Laskar is with the Georgia Institute of Technology, School of Electrical and Computer Engineering, Atlanta, GA 30332-0250 USA.
J. J. Bautista is with Jet Propulsion Laboratory, California Institute of Technology, Pasadena, CA 91109-8099 USA.
M. Nishimoto, M Hamai, and R. Lai are with TRW Electronics Systems and Technology Division, Redondo Beach, CA 90278 USA.

Publisher Item Identifier S 0018-9480(96)04728-X.